

Elucidating image-to-set prediction: An analysis of models, losses and datasets

Luis Pineda^{1*} Amaia Salvador^{2*†} Michal Drozdal¹ Adriana Romero¹

¹Facebook AI Research ²Universitat Politècnica de Catalunya

amaia.salvador@upc.edu, {lep, mdrozdal, adrianars}@fb.com

Abstract

In recent years, we have experienced a flurry of contributions in the multi-label classification literature. This problem has been framed under different perspectives, from predicting independent labels, to modeling label co-occurrences via architectural and/or loss function design. Despite great progress, it is still unclear which modeling choices are best suited to address this task, partially due to the lack of well defined benchmarks. Therefore, in this paper, we provide an in-depth analysis on five different computer vision datasets of increasing task complexity that are suitable for multi-label classification (VOC, COCO, NUS-WIDE, ADE20k and Recipe1M). Our results show that (1) modeling label co-occurrences and predicting the number of labels that appear in the image is important, especially in high-dimensional output spaces; (2) carefully tuning hyper-parameters for very simple baselines leads to significant improvements, comparable to previously reported results; and (3) as a consequence of our analysis, we achieve state-of-the-art results on 3 datasets for which a fair comparison to previously published methods is feasible.

1. Introduction

Among all image understanding tasks [21, 44, 14, 37, 36, 30, 18, 13, 3], image classification has arguably received most of the attention in computer vision, leading to the development of neural network architectures that reach super-human performance on some datasets (e.g. the classification test error on the ImageNet dataset [40] is now far below 5% [14]). However, images taken in-the-wild rarely contain a single object, as everyday life pictures are typically complex scenes, which are inherently multi-label. Although tasks such as object detection or semantic segmentation already account for this increased scene complexity, they require detailed annotations, which are usually expensive to obtain. Nevertheless, multi-label annotation is a go-to standard in many social networks platforms (e.g. hash-

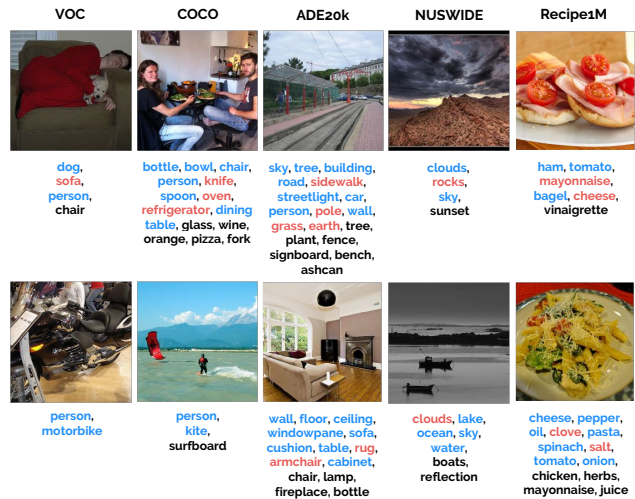


Figure 1: Qualitative results. Each column includes two examples for each dataset. True positives, false positives and false negatives are highlighted in **blue**, **red** and **black**, respectively.

tags) [32] and thus, it equips the research community with large amounts of weak annotations of numerous concepts.

Multi-label classification can be naturally framed as an image-to-set prediction problem, since image labels may exhibit relevant dependencies and the number of labels per image is variable. However, many multi-label classification approaches assume constant set cardinality across images in the dataset [12, 57, 7, 49, 48, 23, 27] and/or are oblivious to label co-occurrences [61, 38, 39]; only a few papers model both characteristics of the image-to-set prediction task [24]. Therefore, there is a need to systematically inquire about the importance of modeling co-occurrences among set elements as well as predicting set cardinality.

Another important question is the image-to-set dataset choice, as different datasets are characterized by different levels of label dependencies and different set cardinality distributions. The most widely used datasets for this task are adapted versions of object detection datasets (Pascal VOC [11], MS COCO [25]) or hashtag prediction datasets (NUS-WIDE [8]). Object detection-based datasets contain fully or partially visible object classes exclusively (e.g.

*Equal contribution.

†Work partially done during internship at Facebook AI Research.

dog, table), whereas hashtag prediction datasets may contain classes with higher degree of abstraction (e.g. soccer, party). Moreover, all these datasets have a rather limited number of possible classes (below 100) and a small number of annotations per image (less than 3 on average). Therefore, there is a need to consider more challenging datasets in terms of: (1) class abstraction, (2) number of classes, and (3) number of labels per image. In addition to that, there seems to be no clear consensus among researchers on the metrics to report. On the one hand, some papers report performance in terms of mean average precision [50, 51, 55] (reminiscent of object detection) while, on the other hand, others consider intersection-over-union based metrics such as F1 score [12, 24, 57, 7, 6, 49, 48, 61, 38, 39].

The lack of benchmarks with well defined metrics and the rather constrained datasets may hinder the fair comparison between existing methods and slow down advances in the field. Therefore, in this paper, we argue for a standardized approach to the problem of image-to-set of labels prediction, and present an extensive study of neural network architectures (including feed forward and auto-regressive ones) as well as loss functions (covering binary cross-entropy, soft intersection-over-union, target distribution and cross-entropy) for multi-label classification. We explore different ways of explicitly accounting for class co-occurrences (either through the model architecture or specific loss functions) as well as determining the set cardinality. We compare all tested approaches on five datasets of increasing task complexity, namely Pascal VOC 2007 [11], MS COCO 2014 [25], ADE20k [60], NUS-WIDE [8] and Recipe1M [42] and benchmark all methods in terms of a unified evaluation framework, while ensuring proper and efficient hyperparameter search through the Hyperband algorithm [22]. We make the code, best models and dataset splits publicly available at: <http://anonymous.url>¹.

The contributions of this paper can be summarized as:

- We provide an in-depth analysis of the current landscape of image-to-set prediction models, in terms of architectures, loss functions, and their treatment of co-occurrences and set cardinality prediction.
- We evaluate these models using a unified set of metrics on 5 datasets of varying degrees of complexity. Moreover, by carrying extensive hyperparameter tuning for all models, we ensure that differences in performance can be attributed to modeling choices, rather than incomplete hyperparameter optimization.
- Our analysis leads to models that reach state-of-the-art performance on the datasets for which a fair comparison to previous methods is possible.

Our results indicate that auto-regressive models outperform feed-forward ones, with the former models consistently being among the top performers on all of the

datasets. This suggests that accounting jointly for both co-occurrences and set cardinality is beneficial. Interestingly, a simple feed-forward network trained with binary cross-entropy loss is also a reasonably good performer in most datasets, reinforcing the importance of proper hyperparameter tuning of baseline models.

2. Related Work

Multi-label classification has been a long lasting problem in computer vision [58, 16, 59, 54]. Traditionally, the problem has been tackled from many different perspectives, from decomposing the problem into independent binary predictions [33, 58] or modeling label correlations [1, 43, 28], to exploiting priors such as label noise and sparsity [16, 19, 45, 54, 59, 2]. More recently, significant effort has been devoted to leveraging deep neural networks for multi-label classification. Approaches in the deep learning realm often use pre-trained (single-label) image classification models (such as VGG [44] or ResNet [14]) as image feature extractors. Then, they decompose the multi-label classification problem into independent single-label classification problems, by either independently classifying features extracted locally from object proposals [55, 51, 29] or by considering global image features and finetuning the pre-trained models with a binary logistic loss [5, 4, 61]. By considering object proposals separately, the former approaches fail to consider potentially relevant object co-occurrence information. However, the latter approaches could implicitly exploit object co-occurrences from the image global features when deciding on each individual class. Yet, by using a per-class binary logistic loss, these models inherently assume independence among labels.

In order to explicitly capture label co-occurrences, powersets [46] and methods learning the joint probability distribution of labels have been introduced in the literature. Although effective, such methods consider all possible label combinations, and thus can quickly become intractable. To overcome the scalability shortcoming while still modeling label co-occurrences, probabilistic classifier chains [9] and recurrent neural network-based approaches [48, 34, 23, 27] decompose the joint distribution into conditionals at the expense of introducing intrinsic label ordering during training. Therefore, recent works propose to train recurrent neural network-based models either by applying a category-wise max-pooling across the time dimension prior to computing the loss [49, 7, 57, 41] or by optimizing for the most likely ground truth label at each time step [6], effectively getting rid of any enforced order. Other solutions to capture label co-occurrences include learning joint input and label embeddings with ranking-based losses [53, 26, 56, 24, 12] as well as designing loss functions such as target distribution mean squared error [50] or target distribution cross-entropy [12, 32, 41], which directly account for those.

¹Coming soon!

Model	#outputs	Loss	Dependencies	Cardinality
FF	1	BCE	-	prob. th
FF	1	sIoU	\mathcal{L}	prob. th
FF	1	TD	\mathcal{L}	cum. prob. th
FF	2	BCE	-	DC dist.
FF	2	BCE	-	C dist.
FF	2	sIoU	\mathcal{L}	C dist.
FF	2	TD	\mathcal{L}	C dist.
LSTM	\hat{K}	CE	θ	<i>eos</i> token
LSTM _{set}	\hat{K}	BCE	θ	<i>eos</i> token
TF	\hat{K}	CE	θ	<i>eos</i> token
TF _{set}	\hat{K}	BCE	θ	<i>eos</i> token

Table 1: Models summary. Loss-based modeling of label co-occurrences is denoted with \mathcal{L} , while explicitly modeling dependencies in the architecture is represented by θ . Notation: FF (feed-forward), LSTM (long short-term memory), TF (transformer), BCE (binary cross-entropy), sIoU (soft intersection-over-union), TD (target distribution), CE (categorical cross-entropy), DC dist. (Dirichlet-Categorical) and C dist. (Categorical distribution).

Finally, most state-of-the-art methods are not concerned with estimating the number of labels to be predicted (set cardinality). Instead, they care about evaluating their top- k predictions [12, 57, 7, 49, 48], by manually fixing k for all samples, or apply a fixed threshold to label probabilities [61, 5] (allowing for different number of images per sample). Only recently, multi-label classification has been explicitly addressed as a set prediction problem, where both labels and cardinality are predicted. This is the case of [38, 39, 24], which model set cardinality as a categorical distribution, [24], which learns class-specific probability thresholds, and [52], which treats set prediction as a parameterized policy search problem.

3. Image-to-Set Prediction Methods

In image-to-set prediction, we are given a dataset of image and set of labels pairs, with the goal of learning to produce the correct set of labels given an image. The set of labels is an unordered collection of unique elements, which may have variable size. Let $\mathcal{D} = \{d_i\}_{i=1}^N$ be a dictionary of labels of size N , from which we can obtain the set of labels S for an image \mathbf{x} by selecting $K \geq 0$ elements from \mathcal{D} . If $K = 0$, no elements are selected and $S = \{\}$; otherwise $S = \{s_i\}_{i=1}^K$. Thus, our training data consists of M image and label pairs $\{(\mathbf{x}^{(i)}, S^{(i)})\}_{i=1}^M$.

Table 1 gives an overview of the image-to-set prediction models considered in this study. A comprehensive overview of set prediction models is out of the scope of this paper; we limit the scope of our study to approaches based on feed forward (FF) architectures as well as auto-regressive ones, since they are currently the state-of-the-art for this task. Overall, the models we consider can be categorized according to: (1) whether they model co-occurrences of elements in the set, and (2) whether they explicitly model set

cardinality. All models are composed of an image representation module, followed by a set prediction module, which are stacked together and trained end-to-end.

Image Representation. We choose ResNet-50 [14] as image encoder, initialized with pre-trained ImageNet [40] weights, given its ubiquitous role in the literature. The encoder transforms an input image $\mathbf{x} \in \mathbb{R}^{W \times H \times 3}$ into a representation $\mathbf{r} = f_\phi(\mathbf{x})$ of dimensions $w \times h \times 2048$, where w and h are the width and height of the convolutional features, respectively.

Set Prediction. In this paper, we consider feed-forward and auto-regressive architectures for image-to-set prediction, which are described in the following subsections.

3.1. Feed-forward Models

Notation: We represent S as a binary vector \mathbf{s} of dimension N , where $s_i = 1$ if $s_i \in S$ and 0 otherwise². The goal is to estimate the label probabilities $\hat{\mathbf{s}}$ from an image \mathbf{x} . Training data consists of M image and set pairs.

Architectures: Feed-forward models take image features \mathbf{r} as input and output $\hat{\mathbf{s}} = g_\theta(\mathbf{r})$. These models are composed of (1) an optional 1×1 convolutional block to change the feature dimensionality of the input features, (2) a global average pooling operation to collapse the spatial dimensions, and (3) one or more fully connected layers. Intermediate fully connected layers are followed by dropout, batch normalization and a ReLU non-linearity. The last fully connected layer serves as classifier, and thus, is followed by a sigmoid non-linearity to obtain the vector of estimated probabilities. The architecture used for all feed-forward models is depicted in Figure 2a.

Loss functions: The model’s parameters are trained by maximizing the following objective over the dataset:

$$\arg \max_{\phi, \theta} \sum_{i=0}^M \log p(\hat{\mathbf{s}}^{(i)} = \mathbf{s}^{(i)} | \mathbf{x}^{(i)}; \phi, \theta). \quad (1)$$

where ϕ and θ are the image representation and set predictor parameters, respectively. Most state-of-the-art feed-forward methods assume independence among labels, factorizing $p(\hat{\mathbf{s}}^{(i)} = \mathbf{s}^{(i)} | \mathbf{x}^{(i)})$ as $\sum_{j=0}^N \log p(\hat{s}_j^{(i)} = s_j^{(i)} | \mathbf{x}^{(i)})$ and using binary cross-entropy (BCE) as training loss. However, the elements in the set are not necessarily independent. Therefore, we can borrow from the semantic segmentation literature and train the feed-forward set predictor with a soft structured prediction loss, such as the soft intersection-over-union (sIoU) [10], in order to take into account dependencies among elements in the set. Alternatively, we can use the *target distribution* $p(\mathbf{s}^{(i)} | \mathbf{x}^{(i)}) = \mathbf{s}^{(i)} / \sum_j \mathbf{s}_j^{(i)}$ [12, 32] to model the joint distribution of set elements and train a model by minimizing the cross-entropy loss between

²Recall that N represents the size of the label dictionary.

$p(\mathbf{s}^{(i)}|\mathbf{x}^{(i)})$ and the model’s output distribution $p(\hat{\mathbf{s}}^{(i)}|\mathbf{x}^{(i)})$. Hereinafter, we refer to the feed-forward model trained with BCE as FF_{BCE} , the one trained with sIoU as FF_{sIoU} , and the one trained with target distribution as FF_{TD} .

Set cardinality: Given the estimated probabilities $\hat{\mathbf{s}}$ obtained with any of the aforementioned approaches, a set of labels \hat{S} must be recovered. For both FF_{BCE} and FF_{sIoU} , one simple solution is to apply a threshold th to $\hat{\mathbf{s}}$, keeping all labels for which $\hat{s}_i \geq th$. Typically, this threshold is set to 0.5. Nonetheless, in the case of the FF_{TD} , we adopt the strategy of [41] and recover the label set by greedily sampling elements from a *cumulative distribution of sorted output probabilities* $p(\hat{\mathbf{s}}^{(i)}|\mathbf{x}^{(i)})$ and stop the sampling once the sum of probabilities of selected elements is above a threshold $th = 0.5$. Alternatively, the set cardinality K may be explicitly predicted by the feed-forward model through a second output $\hat{\mathbf{K}}, \hat{\mathbf{K}} = g_\theta(\mathbf{r})$, where $\hat{\mathbf{K}}$ represents the categorical distribution over possible set cardinalities. At inference time, the top- \hat{K} labels with highest probability are included in the predicted set. For completeness, in our experiments we also use a variant of FF_{BCE} where the set cardinality is modeled with Dirichlet-Categorical distribution, following the model described in [39].

Empty set prediction: Images with missing labels (i.e., $S = \{\}$) can be naturally handled by models that assume label independence (e.g. FF_{BCE} and FF_{sIoU} , whose output is a probability distribution for each label). At inference time, the set cardinality is predicted implicitly by applying a threshold value th to each output probability. The set cardinality can be also modeled explicitly (through a second output), where the output of cardinality 0 corresponds to empty set. From the feed-forward models considered, only FF_{TD} cannot handle empty sets, since a vector with all zeros is not a valid (categorical) probability distribution.

3.2. Auto-regressive Models

Notation: When using auto-regressive models, we represent S as a binary matrix \mathbf{S} of dimensions $K \times N$.³ We set $\mathbf{S}_{i,j} = 1$ if label d_j is selected at i -th position and 0 otherwise (in other words, each row in \mathbf{S} contains the one-hot-code representation of one label).

Architectures: We explore two auto-regressive architectures, namely a Long Short-Term Memory (LSTM) [15] with spatial attention-based model [31] and a transformer-based (TF) one [47]. Both LSTM and TF take image features \mathbf{r} as input and output $\hat{\mathbf{S}} = g_\theta(\mathbf{r})$. These models are composed of (1) an optional 1×1 convolutional block to change the feature dimensionality of the input features, and (2) either a single LSTM layer (following [31]) or several transformer layers (following [47, 41]). The output layer of the model is used as classifier and has a softmax non-

³Recall that K defines the set cardinality and N the size of the dictionary of possible labels.

linearity. These models predict one element of the set at each time-step. The LSTM and Transformer architectures are depicted in Figures 2b and 2c, respectively.

Loss functions: In this scenario, the goal is to predict $\hat{\mathbf{S}}$ from an image \mathbf{x} by maximizing the following objective.

$$\arg \max_{\phi, \theta} \sum_{i=0}^M \log p(\hat{\mathbf{S}}^{(i)} = \mathbf{S}^{(i)} | \mathbf{x}^{(i)}; \phi, \theta), \quad (2)$$

To ensure that labels in $\hat{\mathbf{S}}^{(i)}$ are selected without repetition, we force the pre-activation of $p(\hat{\mathbf{S}}_k^{(i)} | \mathbf{x}^{(i)}, \mathbf{S}_{<k}^{(i)})$ to be $-\infty$ for all previously selected labels at time-steps $< k$. One characteristic of the formulation in Equation 2 is that it inherently penalizes for order, which might not necessarily be relevant for the set prediction task. In order to ignore the order in which labels are predicted, we employ the solution of [41] and aggregate the outputs across different time-steps by means of a max pooling operation. In this case, instead of minimizing the cross-entropy error at each time step, we minimize the BCE between the pooled predicted labels and the ground truth. Hereinafter, we refer to the LSTM and TF models trained with pooled time-steps as LSTM_{set} and TF_{set} , respectively. It is worth noting that, in all cases, at inference time, we directly sample from the auto-regressive predictor’s output.

Set cardinality: Most auto-regressive set predictors in the literature are not concerned with cardinality prediction, and predict a fixed number of elements by default [7, 48]. However, we argue that those models inherently have the mechanism to learn when to stop. Therefore, as commonly done in tasks such as image captioning and machine translation, we introduce an end-of-sequence *eos* token to the dictionary of labels, which has to be predicted in the last sequence step. Thus, in our case, the *eos* token’s role is to estimate the cardinality of the set. In the case of LSTM_{set} and TF_{set} , we learn the stopping criterion with an additional loss accounting for it. The *eos* loss is defined as the BCE loss between the predicted *eos* probability at all time-steps and the ground truth (represented as a unit step function, whose value is 0 for the time-steps corresponding to labels and 1 otherwise). In addition to that, we incorporate the cardinality ℓ_1 penalty of [41]. In this last case, we weight the contribution of the *eos*-loss and cardinality penalty terms with hyperparameters λ_{eos} and λ_{CP} , respectively.

Empty set prediction: We handle images with missing labels by setting the *eos* token as the first element to be predicted in the sequence.

4. Experiments

4.1. Datasets and Metrics

We train and evaluate our models on five different image datasets, which provide multi-label annotations. The

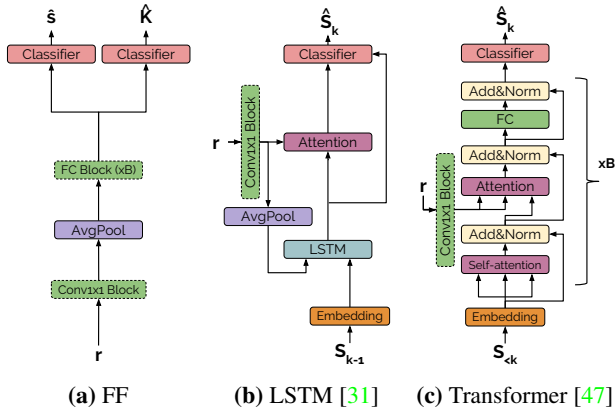


Figure 2: Set prediction architectures. (a) Feed-forward (FF), (b) LSTM and (c) Transformer. Dashed lines denote optional blocks.

dataset details are presented in Table 2, while the distribution of the training set cardinality is depicted in Figure 3.

Pascal VOC 2007 [11] is a popular benchmark for image classification, object detection and segmentation tasks. It is composed of 9 963 images containing objects from 20 distinct categories. Images are divided in 2 501, 2 510 and 4 952 for train, validation and test splits, respectively. We train with 90% of the *trainval* images, keeping 10% for validation. Models are evaluated on the test set, for which annotations have been released.

MS COCO 2014 [25] is a popular benchmark for object detection and segmentation on natural images, containing annotations for objects of 80 different categories. It is composed of 82 783 images for training and 40 504 for validation. Since evaluation on the test set can only be done through the benchmark server, which currently does not support the set prediction task, we use 10% of the training set for validation, and evaluate on the full validation set. Note that in our experiments we include images with no annotations as *empty sets*.

NUS-WIDE [8] is a web image database composed of 161 789 images for training and 107 859 for testing, annotated with 81 unique tags collected from Flickr. While VOC and MS COCO are annotated with visually grounded object tags (e.g. *dog*, *train* or *person*), NUS-WIDE includes a wider variety of tags referring to activities (e.g. *wedding*, *soccer*), scenes (e.g. *snow*, *airport*) and objects (e.g. *car*, *computer*, *dog*). As in COCO, this dataset includes images with *empty sets* annotations.

ADE20k [60] is a scene parsing dataset, containing 20 210 training, 2 000 validation samples, annotated with a dictionary of 150 labels. Since the test set server evaluation is not suited for image to set prediction, we use validation set as a test set and separate a new validation set from the training set. As a result we obtain 18 176, 2 020 and 2 000 images for train, validation and test splits, respectively.

	VOC	COCO	NUS-WIDE	ADE20k	Recipe1M
Train	4 509	74 503	145 610	18 176	252 547
Val	502	8 280	16 179	2 020	5 000
Test	4 952	40 504	107 859	2 000	54 506
N	20	80	81	150	1 486
K	1.57 (0.77)	2.91 (1.84)	1.86 (1.71)	8.17 (4.14)	7.99 (3.21)

Table 2: Splits, dictionary size (N), and cardinality (K), reported as *mean (std)* for each dataset.

Recipe1M [42] composed of 1 029 720 recipes scraped from cooking websites. The dataset is split in 720 639 training, 155 036 validation and 154 045 test samples, each containing a cooking recipe (from which we only use ingredients) and (optionally) images. In our experiments, we use only those samples containing images. Following [41], we pre-process the ingredient dictionary by (1) removing plurals, (2) clustering together ingredients that share the first or last two words, (3) merge ingredients sharing the first or last word, (4) removing infrequent ingredients (appearing less than 10 times), and (5) remove recipes with less than 2 ingredients. This procedure results in 1 486 unique ingredients and 252 547 training, 54 255 validation and 54 506 test samples. To speed up the training, we use 5 000 randomly chosen validation images.

Metrics. We evaluate all methods by means of F1 score calculated per-class (C-F1), per-image (I-F1) and overall (O-F1). Note that O-F1 and C-F1 are also commonly referred to as macro- and micro-F1, respectively.

4.2. Implementation details

We resize all images to 448 pixels in their shortest side, preserving aspect ratio, and take random crops of 448×448 for training. We randomly flip ($p = 0.5$), translate (within a range of $\pm 10\%$ of the image size on each axis) and rotate images ($\pm 10^\circ$) for data augmentation during training. All models are trained with the Adam optimizer [20] for a maximum of 200 epochs, or until early-stopping criterion is met (monitoring the O-F1 metric and using patience of 50 epochs for VOC and 10 epochs for the remaining datasets). All models are implemented with PyTorch⁴ [35]. For autoregressive models, we train on two variants of annotations: (1) we keep the dataset order (e. g. LSTM and TF), and (2) we randomly shuffle the labels each time we load an image (e. g. LSTM_{shuffle} and TF_{shuffle}). Additional implementation details and final hyperparameter values for each of the models are provided in the supplementary material, together with the hyperparameters ranges considered and an analysis of the explored hyperparameter space.

⁴<http://pytorch.org/>

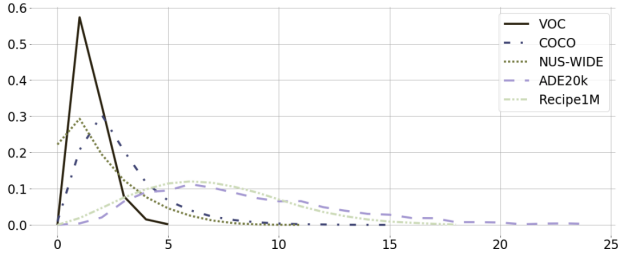


Figure 3: Dataset cardinality distribution.

4.3. Model selection

To tune all model hyperparameters, we used HYPERBAND [22], a bandit-based algorithm that speeds up random search via an aggressive form of early-stopping called SUCCESSIVEHALVING [17]. In SUCCESSIVEHALVING, a set of n different hyperparameter combinations is sampled, each of which is initially allowed to run using r “resources” (e.g., training time, some number of epochs, size used for dataset subsampling). The best n/η of these are kept (according to best O-F1 over validation set observed after using r resources) and subsequently run with ηr resources, where η is a parameter controlling the rate at which values are discarded; this elimination process is repeated until a single best configuration is chosen. However, since SUCCESSIVEHALVING might be too aggressive (i.e., it can discard potentially good configurations in early steps), HYPERBAND hedges by repeating the process multiple times. Each repetition—or “bracket”—uses different hyperparameters n and resource limits r to control the level of aggressiveness; moreover, these values are chosen so that the total resource usage across all runs in each bracket is approximately uniform. This approach has theoretical guarantees that don’t rely on strong assumptions about the function to be optimized (in our case best O-F1 over validation set). Moreover, it has been shown to result in substantial computational savings with respect to a random search that does not use SUCCESSIVEHALVING [22]. In our experiments, we used $\eta = 3$, and a maximum value of r equal to $R = 600$, where each resource unit is equivalent to 0.15 training epochs for most datasets, rounding up when necessary (for VOC, equivalent to 0.2 epochs). This translates to roughly 410 hyperparameter configurations evaluated per model, and a maximum budget of 3 200 epochs (4 400 for VOC) for the complete tuning process (with at most 90 training epochs per model); note that we also used patience for monitoring the O-F1 metric during tuning, so this budget is an upper bound. We used the same random seed for all models instantiated during the tuning process.

4.4. Analysis

Set label prediction. Table 3 reports results for all models and datasets in terms of O-F1, C-F1 and I-F1 metrics. Note that each experiment was run with 5 different seeds

(different from the one used for hyper-parameter selection), and thus we report the mean and standard deviation results of each model. Models appear following their average normalized O-F1 score over all datasets (O-F1 scores are normalized using the maximum O-F1 of the corresponding dataset). According to the ranking, auto-regressive models outperform feed-forward ones. This suggests that explicitly considering both label co-occurrences and set cardinality while training is favorable. Surprisingly, a well tuned very simple baseline (FF_{BCE}) achieves a reasonably high ranking, beating all other feed-forward models.

For VOC dataset, FF_{sIoU} achieves the best performance among feed-forward models, reaching 87.19 O-F1, and closely followed by FF_{BCE} (86.50 O-F1). Interestingly, their feed-forward counterparts predicting set cardinality achieve slightly worse performance. When it comes to auto-regressive set predictors, $LSTM_{shuffle}$ trained with shuffled labels achieves the best performance with an O-F1 score of 87.36, whereas the rest of these models obtain performances within 1.5 points of $LSTM_{shuffle}$. In the case of COCO dataset, $LSTM_{shuffle}$ is the best performing model (77.19 O-F1), followed by $TF_{shuffle}$ and TF . The best feed-forward model for this dataset is FF_{BCE} (76.57 O-F1). Contrary to VOC, auto-regressive models generally outperform feed-forward ones on COCO and, once again, we observe a drop in performance when predicting cardinality in feed-forward models. In the case of NUS-WIDE, auto-regressive models (TF and $LSTM$) lead the results. It is worth noting that models trained to exploit the dataset order of labels perform better than those trained with shuffled ones. This is not surprising since the label’s order in NUS-WIDE is consistent across all data points (it follows alphabetical order). Similarly to COCO dataset, FF_{BCE} is the best performing feed-forward model, and most of the feed-forward models which predict cardinality are among the least performing ones. When it comes to ADE20k, FF_{BCE} achieves the best performance, with an O-F1 of 70.66 O-F1. In contrast to the previous datasets, endowing feed-forward models with a cardinality prediction path tends to have a rather neutral effect. Most auto-regressive models also exhibit good performance in this dataset. While FF_{BCE} and $LSTM$ perform comparably in terms of O-F1, $LSTM$ reaches better C-F1 (48.67 vs 48.00) than FF_{BCE} . It is worth mentioning that, as in NUS-WIDE, label order is consistent across samples, and thus can be exploited. Finally, in Recipe1M, $FF_{TD,C}$ has the best overall performance (49.94). Predicting cardinality seems to help some feed-forward models in this dataset; this is the case of $FF_{TD,C}$ but also $FF_{BCE,C}$. Except for FF_{sIoU} and $FF_{sIoU,C}$, explicitly taking advantage of class co-occurrences seems to be beneficial. We hypothesize that this is due to the nature of the dataset, which entails more abstract classes requiring reasoning beyond the merely visible. It is worth highlight-

Rank	Model	VOC			COCO			NUS-WIDE			ADE20k			Recipe1M		
		O-F1	C-F1	I-F1	O-F1	C-F1	I-F1	O-F1	C-F1	I-F1	F1	C-F1	I-F1	O-F1	C-F1	I-F1
1	TF _{shuffle}	86.76 (0.25)	85.66 (0.30)	88.55 (0.26)	77.12 (0.06)	73.72 (0.07)	80.00 (0.06)	69.21 (0.21)	53.23 (0.75)	66.80 (0.75)	70.31 (0.18)	46.41 (0.68)	69.62 (0.12)	48.43 (0.08)	19.37 (0.32)	46.99 (0.10)
2	TF	85.79 (0.26)	84.16 (0.42)	87.78 (0.21)	76.91 (0.06)	73.71 (0.11)	79.69 (0.04)	70.81 (0.02)	55.56 (0.11)	69.47 (0.03)	70.29 (0.20)	47.44 (0.34)	69.16 (0.26)	47.53 (0.02)	17.98 (0.06)	46.20 (0.04)
3	LSTM	86.36 (0.15)	84.77 (0.37)	88.23 (0.13)	76.66 (0.06)	73.04 (0.07)	79.47 (0.06)	70.60 (0.08)	53.22 (0.49)	68.71 (0.21)	70.60 (0.21)	48.67 (0.86)	69.96 (0.21)	47.22 (0.06)	17.57 (0.03)	45.75 (0.07)
4	LSTM _{shuffle}	87.36 (0.37)	85.87 (0.51)	89.07 (0.30)	77.19 (0.06)	73.68 (0.09)	80.07 (0.04)	68.08 (0.14)	49.70 (0.69)	63.25 (0.83)	69.56 (0.30)	43.13 (0.86)	68.98 (0.35)	47.62 (0.10)	16.84 (0.03)	45.98 (0.10)
5	LSTM _{set}	86.09 (0.11)	85.12 (0.10)	87.99 (0.12)	76.23 (0.10)	72.70 (0.15)	79.21 (0.06)	69.88 (0.17)	55.38 (0.24)	67.65 (0.32)	70.27 (0.65)	47.44 (2.32)	69.51 (0.55)	45.43 (0.67)	16.72 (0.21)	43.47 (0.66)
6	FF _{BCE}	86.50 (0.17)	85.22 (0.15)	88.36 (0.17)	76.57 (0.05)	72.80 (0.07)	78.67 (0.05)	68.92 (0.05)	53.32 (0.10)	56.29 (0.08)	70.66 (0.37)	48.00 (0.30)	69.28 (0.41)	45.02 (0.09)	17.58 (0.08)	41.60 (0.09)
7	FF _{BCE,DC}	85.74 (0.39)	83.97 (0.38)	87.88 (0.33)	75.95 (0.07)	71.86 (0.12)	77.98 (0.07)	68.39 (0.11)	52.38 (0.23)	55.59 (0.11)	70.65 (0.13)	46.04 (0.58)	69.93 (0.14)	42.96 (1.56)	14.31 (1.02)	40.83 (1.66)
8	FF _{TD,C}	84.79 (0.22)	83.57 (0.36)	87.03 (0.17)	70.93 (0.12)	68.83 (0.15)	69.73 (0.13)	63.79 (0.05)	47.97 (0.81)	49.98 (0.05)	69.39 (0.23)	48.31 (0.49)	68.49 (0.19)	49.94 (0.07)	18.92 (0.19)	48.48 (0.07)
9	FF _{BCE,C}	84.68 (0.08)	84.14 (0.17)	86.84 (0.08)	70.42 (0.25)	68.18 (0.26)	69.00 (0.37)	62.42 (0.27)	45.74 (1.55)	49.14 (0.30)	70.13 (0.11)	43.72 (0.29)	69.06 (0.14)	49.18 (0.01)	17.66 (0.08)	47.36 (0.01)
10	TF _{set}	86.31 (0.12)	85.05 (0.26)	88.13 (0.11)	75.10 (1.24)	71.33 (1.75)	78.07 (1.13)	57.90 (26.28)	43.71 (23.51)	55.83 (25.63)	70.11 (0.28)	50.16 (0.48)	69.21 (0.31)	47.54 (0.62)	18.90 (0.11)	45.60 (0.69)
11	FF _{sIoU}	87.19 (0.07)	85.90 (0.13)	89.16 (0.09)	73.21 (0.69)	59.93 (1.43)	74.55 (0.79)	62.39 (0.40)	12.84 (0.53)	51.24 (0.21)	67.64 (0.21)	20.82 (0.44)	66.98 (0.22)	44.33 (0.18)	12.79 (0.03)	42.53 (0.18)
12	FF _{sIoU,C}	85.93 (0.09)	84.58 (0.10)	88.04 (0.10)	66.01 (0.42)	52.69 (1.02)	64.26 (0.47)	54.70 (0.45)	9.87 (0.49)	42.54 (0.60)	65.96 (0.21)	20.17 (0.39)	65.06 (0.20)	42.55 (0.30)	12.67 (0.02)	40.36 (0.40)
-	FF _{TD}	79.24 (0.24)	79.05 (0.91)	82.95 (0.18)	-	-	-	-	-	-	64.74 (0.31)	39.33 (0.88)	64.69 (0.36)	47.85 (0.07)	18.34 (0.07)	47.90 (0.06)

Table 3: Results on VOC, COCO, NUS-WIDE, ADE20k and Recipe1M (test set). We report C-F1, O-F1 and I-F1 computed for each model. Models are trained 5 times using different random seeds. We report *mean (std)* for each metric, model and dataset. The models are ordered according to their average normalized O-F1 score computed over all five tested datasets. Note that FF_{TD} is not considered to obtain the mean ranking, since it is not used for datasets including empty sets (COCO and NUS-WIDE).

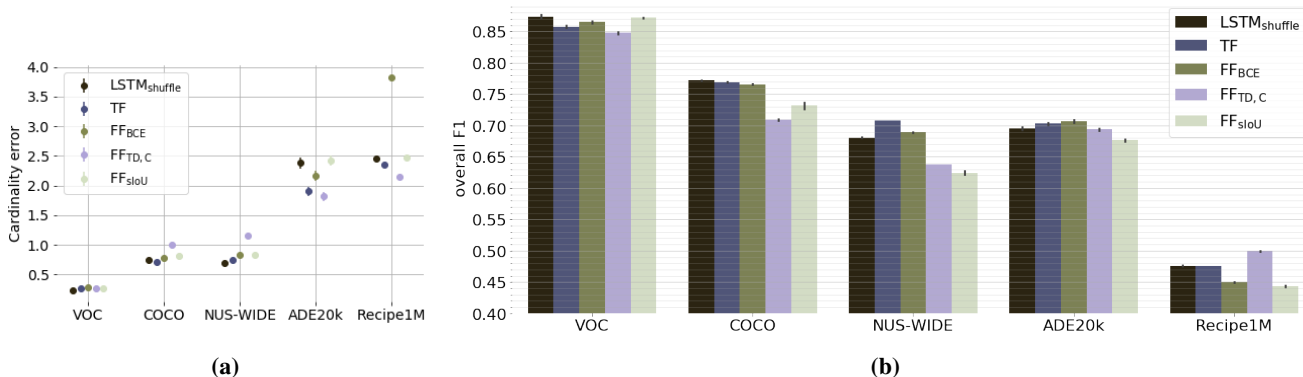


Figure 4: (a): Cardinality error per image on each dataset (mean and 95% confidence interval). (b): O-F1 per dataset (mean and 95% confidence interval computed over 5 seeds). We compare the best models for each tested dataset as well as two standard feed-forward models FF_{BCE} and FF_{sIoU}.

ing the rather low average performance and high standard deviation that TF_{set} displays for the NUS-WIDE dataset. We attribute the high variance to optimization difficulty, since this model is sensitive to initialization and fails to converge for some seeds. Nevertheless, in the cases where the model converges, it is typically among the top perform-

ers, which suggests that it is potentially a good choice for image-to-set prediction if the optimization issues can be addressed. An overview on the order consistency among labels in each dataset is given in the supplementary material.

Figure 4 presents the test O-F1 metric and cardinal-

	COCO	VOC	Recipe1M
Li et al. [24]	62.90	79.10	-
Zhu et al. [61]	75.80	-	-
Liu et al. [29]	74.00	-	-
Liu et al. [38]	69.00	78.60	-
Rezatofghi et al. [39]	70.70	81.50	-
Rezatofghi et al. [57]	66.50	62.90	-
Chen et al. [7]	71.10	-	-
Chen et al. [6]	67.70	-	-
Wang et al. [49]	72.00	-	-
CNN-RNN [48]	67.80	-	-
Li et al. [23]	71.80	-	-
Liu et al. [27]	75.16	-	-
Salvador et al. [41]	-	-	48.66
Ours (best)	77.19	87.37	49.94

Table 4: Comparison to state-of-the-art on COCO, VOC and Recipe1M.

ity prediction errors for the baseline models FF_{BCE} and FF_{sIoU} as well as the models leading to the best performance for each dataset. As shown in the figure, object detection-based datasets appear to be among the easiest ones, achieving higher overall performance and lower cardinality error, with VOC being the easiest dataset and ADE20k the hardest among them. Datasets that contain more abstract annotations and thus, may require higher level reasoning (such as NUS-WIDE and Recipe1M) seem more challenging. Undoubtedly, Recipe1M is the most demanding dataset when it comes to both label and cardinality prediction, as it requires reasoning about non-visible ingredients. As for the model architectures, auto-regressive ones seem to be rather consistent across datasets, exhibiting close to top performances and lower cardinality errors. However, while FF_{IOU} and FF_{BCE} achieve top performance for certain datasets, they experience significant drops when drastically increasing the output dimensionality space (e.g. for Recipe1M there are 1486 possible labels). This performance drop can be attributed to either a higher set cardinality error or wrong label predictions. However, $FF_{TD,C}$ seems to follow a slightly different trend, with improved performance for Recipe1M, the dataset with the largest output dimensionality; this model also achieves notably lower cardinality prediction error than the rest. Interestingly, the tendency of $FF_{TD,C}$'s performance across datasets seems to correlate with the width of the cardinality distribution of the datasets (see Figure 3), experiencing higher O-F1 and lower cardinality error for ADE20k and Recipe1M.

Cardinality Prediction. We compare the best models for each dataset in terms of their performance under different set cardinalities (Figure 5). The x-axis represents the test set annotation cardinality, while y-axis reports the mean I-F1 that corresponds to each given cardinality value. As shown in the figure, predicting empty sets is hard, e.g. for both COCO and NUS-WIDE, the mean I-F1 is significantly lower for images with cardinality 0 than for images of cardinality 1, a pattern that was consistently observed with other

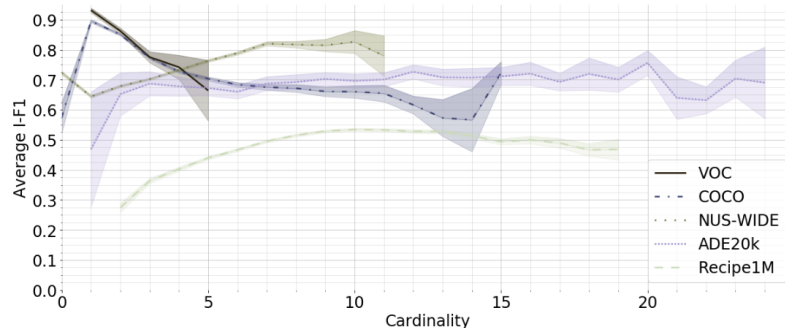


Figure 5: I-F1 as a function of cardinality. We report mean I-F1 and 95% confidence intervals for the best models for each dataset at different cardinality values.

models as well. Moreover, for the datasets that require high level reasoning to predict labels, we observe that I-F1 rises with the set cardinality. We hypothesize that this behavior could be attributed to exploiting co-occurrences that improve label predictions (e.g. the more labels we have, the easier it is to predict a label via reasoning about the co-occurrences).

4.5. Comparison to state-of-the-art

In this subsection, we compare our best models to the state-of-the-art. Table 4 reports the results in terms of O-F1 for VOC, COCO and Recipe1M. Note that state-of-the-art results for NUS-WIDE ignore empty annotations and/or randomly rearrange their splits [6, 61, 24, 27, 29, 23, 57, 12], and thus are not comparable to the results presented in this study. Moreover, to the best of our knowledge, ADE20k has not been used for image-to-set of labels predictions in the past. As shown in the table, we are able to achieve state-of-the-art results in all 3 datasets, even though we challenge our models to predict both the correct labels and the correct set cardinality. This is not the case for the vast majority of methods evaluated on VOC and COCO. Moreover, a well tuned very simple baseline such as FF_{BCE} is able to outperform previous state-of-the-art, achieving 86.50 O-F1 on VOC and 76.57 on COCO, showcasing the importance of proper hyperparameter tuning.

5. Conclusion

In this work, we presented a comprehensive analysis of methods suitable for image-to-set prediction, evaluating their performance in 5 diverse datasets, using uniform set of metrics and budgets for hyperparameter tuning. Our work reviews the current landscape of image-to-set prediction, and helps elucidate the most promising directions for future research. Our analysis suggests that auto-regressive models are better choices than feed-forward models for the task, performing consistently well across all considered datasets. Moreover, we found that, by exploiting standard ideas of

one-to-many sequence models, we can inherently handle set cardinality prediction, label co-occurrences and images without annotations. Additionally, our work emphasizes the importance of thorough hyperparameter tuning, showing that even simple baselines can achieve close to state-of-the-art performance when properly tuned. Finally, we provide all source code, dataset splits and trained models, which can serve as valuable benchmarks to ground future research.

Acknowledgements

The authors would like to thank Joelle Pineau and Mike Rabbat for useful discussions and support.

References

- [1] A. Antonucci, G. Corani, D. D. Mauá, and S. Gabaglio. An ensemble of bayesian networks for multilabel classification. In *IJCAI*, 2013. [2](#)
- [2] W. Bi and J. T. Kwok. Efficient multi-label classification with many labels. In *ICML*, 2013. [2](#)
- [3] A. Casanova, G. Cucurull, M. Drozdal, A. Romero, and Y. Bengio. On the iterative refinement of densely connected representation levels for semantic segmentation. In *CVPR-W*, 2018. [1](#)
- [4] K. Chatfield, K. Simonyan, A. Vedaldi, and A. Zisserman. Return of the devil in the details: Delving deep into convolutional nets. *BMVC*, 2014. [2](#)
- [5] J.-J. Chen and C.-W. Ngo. Deep-based ingredient recognition for cooking recipe retrieval. In *ACM Multimedia*, 2016. [2, 3](#)
- [6] S.-F. Chen, Y.-C. Chen, C.-K. Yeh, and Y.-C. F. Wang. Order-free rnn with visual attention for multi-label classification. In *AAAI*, 2018. [2, 8](#)
- [7] T. Chen, Z. Wang, G. Li, and L. Lin. Recurrent attentional reinforcement learning for multi-label image recognition. In *AAAI*, 2018. [1, 2, 3, 4, 8](#)
- [8] T.-S. Chua, J. Tang, R. Hong, H. Li, Z. Luo, and Y. Zheng. Nus-wide: a real-world web image database from national university of singapore. In *ACM Conference on Image and Video Retrieval*, 2009. [1, 2, 5](#)
- [9] K. Dembczyński, W. Cheng, and E. Hüllermeier. Bayes optimal multilabel classification via probabilistic classifier chains. In *ICML*, 2010. [2](#)
- [10] M. Drozdal, E. Vorontsov, G. Chartrand, S. Kadoury, and C. Pal. The importance of skip connections in biomedical image segmentation. In G. Carneiro, D. Mateus, L. Peter, A. Bradley, J. M. R. S. Tavares, V. Belagiannis, J. P. Papa, J. C. Nascimento, M. Loog, Z. Lu, J. S. Cardoso, and J. Cornebise, editors, *Deep Learning and Data Labeling for Medical Applications*, pages 179–187, Cham, 2016. Springer International Publishing. [3](#)
- [11] M. Everingham, L. Van Gool, C. K. Williams, J. Winn, and A. Zisserman. The pascal visual object classes (voc) challenge. *IJCV*, 2010. [1, 2, 5](#)
- [12] Y. Gong, Y. Jia, T. Leung, A. Toshev, and S. Ioffe. Deep convolutional ranking for multilabel image annotation. *CoRR*, abs/1312.4894, 2013. [1, 2, 3, 8](#)
- [13] K. He, G. Gkioxari, P. Dollár, and R. Girshick. Mask r-cnn. In *ICCV*, 2017. [1](#)
- [14] K. He, X. Zhang, S. Ren, and J. Sun. Deep residual learning for image recognition. In *CVPR*, 2016. [1, 2, 3](#)
- [15] S. Hochreiter and J. Schmidhuber. Long short-term memory. *Neural computation*, 1997. [4](#)
- [16] D. J. Hsu, S. M. Kakade, J. Langford, and T. Zhang. Multi-label prediction via compressed sensing. In Y. Bengio, D. Schuurmans, J. D. Lafferty, C. K. I. Williams, and A. Culotta, editors, *NeurIPS*. Curran Associates, Inc., 2009. [2](#)
- [17] K. Jamieson and A. Talwalkar. Non-stochastic best arm identification and hyperparameter optimization. In *AISTATS*, pages 240–248, 2016. [6](#)
- [18] S. Jégou, M. Drozdal, D. Vazquez, A. Romero, and Y. Bengio. The one hundred layers tiramisu: Fully convolutional densenets for semantic segmentation. In *CVPR-W*, 2017. [1](#)
- [19] A. Kapoor, R. Viswanathan, and P. Jain. Multilabel classification using bayesian compressed sensing. In F. Pereira, C. J. C. Burges, L. Bottou, and K. Q. Weinberger, editors, *NeurIPS*. Curran Associates, Inc., 2012. [2](#)
- [20] D. P. Kingma and J. Ba. Adam: A method for stochastic optimization. *CoRR*, abs/1412.6980, 2014. [5](#)
- [21] A. Krizhevsky, I. Sutskever, and G. E. Hinton. ImageNet classification with deep convolutional neural networks. In *NeurIPS*, 2012. [1](#)
- [22] L. Li, K. Jamieson, G. DeSalvo, A. Rostamizadeh, and A. Talwalkar. Hyperband: A novel bandit-based approach to hyperparameter optimization. *JMLR*, 18(185):1–52, 2018. [2, 6](#)
- [23] L. Li, S. Wang, S. Jiang, and Q. Huang. Attentive recurrent neural network for weak-supervised multi-label image classification. In *ACM Multimedia*, 2018. [1, 2, 8](#)
- [24] Y. Li, Y. Song, and J. Luo. Improving pairwise ranking for multi-label image classification. In *CVPR*, 2017. [1, 2, 3, 8](#)
- [25] T.-Y. Lin, M. Maire, S. Belongie, J. Hays, P. Perona, D. Ramanan, P. Dollár, and C. L. Zitnick. Microsoft coco: Common objects in context. In *ECCV*, 2014. [1, 2, 5](#)
- [26] Z. Lin, G. Ding, M. Hu, and J. Wang. Multi-label classification via feature-aware implicit label space encoding. In *ICML*, 2014. [2](#)
- [27] F. Liu, T. Xiang, T. M. Hospedales, W. Yang, and C. Sun. Semantic regularisation for recurrent image annotation. In *CVPR*, 2017. [1, 2, 8](#)
- [28] W. Liu and I. W. Tsang. Large margin metric learning for multi-label prediction. In *AAAI*, 2015. [2](#)
- [29] Y. Liu, L. Sheng, J. Shao, J. Yan, S. Xiang, and C. Pan. Multi-label image classification via knowledge distillation from weakly-supervised detection. In *ACM Multimedia*, 2018. [2, 8](#)
- [30] J. Long, E. Shelhamer, and T. Darrell. Fully convolutional networks for semantic segmentation. In *CVPR*, 2015. [1](#)
- [31] J. Lu, C. Xiong, D. Parikh, and R. Socher. Knowing when to look: Adaptive attention via a visual sentinel for image captioning. In *CVPR*, 2017. [4, 5](#)

- [32] D. Mahajan, R. B. Girshick, V. Ramanathan, K. He, M. Paluri, Y. Li, A. Bharambe, and L. van der Maaten. Exploring the limits of weakly supervised pretraining. *CoRR*, abs/1805.00932, 2018. 1, 2, 3
- [33] J. Nam, J. Kim, E. L. Mencia, I. Gurevych, and J. Fürnkranz. Large-scale multi-label text classification — revisiting neural networks. In *ECMLPKDD*, 2014. 2
- [34] J. Nam, E. Loza Mencia, H. J. Kim, and J. Fürnkranz. Maximizing subset accuracy with recurrent neural networks in multi-label classification. In *NeurIPS*, 2017. 2
- [35] A. Paszke, S. Gross, S. Chintala, G. Chanan, E. Yang, Z. DeVito, Z. Lin, A. Desmaison, L. Antiga, and A. Lerer. Automatic differentiation in pytorch. In *NeurIPS-W*, 2017. 5
- [36] J. Redmon, S. Divvala, R. Girshick, and A. Farhadi. You only look once: Unified, real-time object detection. In *CVPR*, 2016. 1
- [37] S. Ren, K. He, R. Girshick, and J. Sun. Faster R-CNN: towards real-time object detection with region proposal networks. In *NeurIPS*, 2015. 1
- [38] S. H. Rezatofghi, A. Milan, E. Abbasnejad, A. Dick, I. Reid, et al. Deepsetnet: Predicting sets with deep neural networks. In *ICCV*, 2017. 1, 2, 3, 8
- [39] S. H. Rezatofghi, A. Milan, Q. Shi, A. Dick, and I. Reid. Joint learning of set cardinality and state distribution. *AAAI*, 2018. 1, 2, 3, 4, 8
- [40] O. Russakovsky, J. Deng, H. Su, J. Krause, S. Satheesh, S. Ma, Z. Huang, A. Karpathy, A. Khosla, M. Bernstein, A. C. Berg, and L. Fei-Fei. ImageNet Large Scale Visual Recognition Challenge. *IJCV*, 2015. 1, 3
- [41] A. Salvador, M. Drozdal, X. Giró i Nieto, and A. Romero. Inverse cooking: Recipe generation from food images. In *CVPR*, 2019. 2, 4, 5, 8
- [42] A. Salvador, N. Hynes, Y. Aytar, J. Marin, F. Ofli, I. Weber, and A. Torralba. Learning cross-modal embeddings for cooking recipes and food images. In *CVPR*, 2017. 2, 5
- [43] X. Shu, D. Lai, H. Xu, and L. Tao. Learning shared subspace for multi-label dimensionality reduction via dependence maximization. *Neurocomputing*, 2015. 2
- [44] K. Simonyan and A. Zisserman. Very deep convolutional networks for large-scale image recognition. In *ICLR*, 2015. 1, 2
- [45] Y. Song, D. McDuff, D. Vasisht, and A. Kapoor. Exploiting sparsity and co-occurrence structure for action unit recognition. In *FG*. IEEE Computer Society, 2015. 2
- [46] G. Tsoumakas and I. Vlahavas. Random k-labelsets: An ensemble method for multilabel classification. In J. N. Kok, J. Koronacki, R. L. d. Mantaras, S. Matwin, D. Mladenič, and A. Skowron, editors, *ECML*, 2007. 2
- [47] A. Vaswani, N. Shazeer, N. Parmar, J. Uszkoreit, L. Jones, A. N. Gomez, Ł. Kaiser, and I. Polosukhin. Attention is all you need. In *NeurIPS*, 2017. 4, 5
- [48] J. Wang, Y. Yang, J. Mao, Z. Huang, C. Huang, and W. Xu. CNN-RNN: A unified framework for multi-label image classification. In *CVPR*, 2016. 1, 2, 3, 4, 8
- [49] Z. Wang, T. Chen, G. Li, R. Xu, and L. Lin. Multi-label image recognition by recurrently discovering attentional regions. In *ICCV*, 2017. 1, 2, 3, 8
- [50] Y. Wei, W. Xia, J. Huang, B. Ni, J. Dong, Y. Zhao, and S. Yan. CNN: single-label to multi-label. *CoRR*, abs/1406.5726, 2014. 2
- [51] Y. Wei, W. Xia, M. Lin, J. Huang, B. Ni, J. Dong, Y. Zhao, and S. Yan. Hcp: A flexible cnn framework for multi-label image classification. *TPAMI*, 2016. 2
- [52] S. Welleck, Z. Yao, Y. Gai, J. Mao, Z. Zhang, and K. Cho. Loss functions for multiset prediction. In S. Bengio, H. Wallach, H. Larochelle, K. Grauman, N. Cesa-Bianchi, and R. Garnett, editors, *Advances in Neural Information Processing Systems 31*, pages 5783–5792. Curran Associates, Inc., 2018. 3
- [53] J. Weston, S. Bengio, and N. Usunier. Wsabie: Scaling up to large vocabulary image annotation. In *IJCAI*, 2011. 2
- [54] B. Wu, F. Jia, W. Liu, B. Ghanem, and S. Lyu. Multi-label learning with missing labels using mixed dependency graphs. *IJCV*, 2018. 2
- [55] H. Yang, J. Tianyi Zhou, Y. Zhang, B.-B. Gao, J. Wu, and J. Cai. Exploit bounding box annotations for multi-label object recognition. In *CVPR*, 2016. 2
- [56] C. Yeh, W. Wu, W. Ko, and Y. F. Wang. Learning deep latent spaces for multi-label classification. *CoRR*, abs/1707.00418, 2017. 2
- [57] J. Zhang, Q. Wu, C. Shen, J. Zhang, and J. Lu. Multilabel image classification with regional latent semantic dependencies. *IEEE Transactions on Multimedia*, 2018. 1, 2, 3, 8
- [58] M.-L. Zhang and Z.-H. Zhou. Ml-knn: A lazy learning approach to multi-label learning. *Pattern Recogn.*, 40(7), July 2007. 2
- [59] F. Zhao and Y. Guo. Semi-supervised multi-label learning with incomplete labels. In *IJCAI*, 2015. 2
- [60] B. Zhou, H. Zhao, X. Puig, S. Fidler, A. Barriuso, and A. Torralba. Scene parsing through ade20k dataset. In *CVPR*, 2017. 2, 5
- [61] F. Zhu, H. Li, W. Ouyang, N. Yu, and X. Wang. Learning spatial regularization with image-level supervisions for multi-label image classification. In *CVPR*, 2017. 1, 2, 3, 8

6. Implementation Details

For hyperparameter tuning, we allowed Hyperband to sample values from a set of mutually independent categorical distributions, one for each hyperparameter. The hyperparameters considered for all models, and their possible values, are shown in Tables 5 and 6. The hyperparameter values corresponding to the best models found by Hyperband are shown in Tables 7-11.

7. Qualitative Results

Figure 6 includes examples of predicted label sets for images of each of the 5 datasets. Additionally, Figures 7-11 show qualitative comparisons of models FF_{BCE} and $TF_{shuffle}$ on all datasets. We chose these two models for comparison since: 1) $TF_{shuffle}$ is the first ranked model in terms of overall performance, and 2) FF_{BCE} is the simplest baseline and also the highest ranked feed-forward model.

8. Order in label pairs

Figure 12 depicts the order in label pairs for each dataset. The x-axis is normalized for each dataset. For each label pair (A, B) , we compute the number of times that one label precedes the other. Then, we compute order $O = \max(a, b)/(a + b)$, where a accounts for the number of times that A precedes B in the set (and vice versa for b). A value of $O = 0.5$ indicates no order (i.e. A precedes B as often as B precedes A), and a value of 1.0 indicates total order (A always precedes B , or vice versa). In the case of NUS-WIDE and ADE20k, labels always appear in the same order for all samples. For VOC, COCO and Recipe1M, while the plot reveals some degree of order for all label pairs (all values are above 0.5), most values are below 1.0, indicating that label order is not consistent across samples.

9. Capacity of Tuned Models

Figures 13-17 illustrates the capacity of the best models found during the tuning process; in particular, we show the capacity, in terms of base-10 log of the total number of parameters, for the best 10 hyperparameter configurations found for each model. One trend visible in these plots is that the improvement in performance of auto-regressive models cannot be solely explained by having a larger capacity. While this is true for LSTM-based models, which consistently performed better with the highest embedding size, transformer-based models generally performed better with lower capacities. In fact, these results suggest that, for transformer-based models, capacities below our considered range might have achieved better results. On the other hand, for the rest of the models considered, the capacity appears to be less correlated with overall performance.

Hyperparameter	Values
Embedding size	[256, 512, 1 024, 2 048]
Learning rate	$[10^{-4}, 10^{-3}, 10^{-2}]$
Image encoder’s learning rate scale	$[10^{-2}, 10^{-1}]$
Dropout rate	[0, 0.1, 0.3, 0.5]
Weight decay	$[0, 10^{-4}]$

Table 5: Hyperparameters common to all models and their possible values.

Models	L_t	L_f	n_{att}	Weight for cardinality loss	λ_{eos}	λ_{CP}
TF, TF _{shuffle}	[1, 2, 3]	–	[2, 4, 8]	–	–	–
TF _{set}	[1, 2, 3]	–	[2, 4, 8]	–	$[10^{-3}, 10^{-2}, 10^{-1}, 0.5, 1, 10, 100]$	$[0, 10^{-3}, 10^{-2}, 10^{-1}, 0.5, 1, 10, 100]$
LSTM _{set}	–	–	–	–	$[10^{-3}, 10^{-2}, 10^{-1}, 0.5, 1, 10, 100]$	$[0, 10^{-3}, 10^{-2}, 10^{-1}, 0.5, 1, 10, 100]$
FF _{BCE} , FF _{TD} , FF _{sIoU}	–	[0, 1, 2, 3]	–	–	–	–
FF _{BCE,DC}	–	[0, 1, 2, 3]	–	1	–	–
FF _{BCE,C} , FF _{TD,C} , FF _{sIoU,C}	–	[0, 1, 2, 3]	–	$[10^{-3}, 10^{-2}, 10^{-1}, 0.5, 1, 10, 100]$	–	–

Table 6: Model-specific hyperparameters and their possible values. Models not shown don’t have any additional hyperparameters besides those in Table 5. L_t and L_f represent the number of transformer layers and fully connected layers, respectively, while n_{att} represents the number of attention heads.

Model	L_t	L_f	embedding size	n_{att}	l_r	w_C	λ_{eos}	λ_{CP}	scale	dropout rate	weight decay
TF	3	–	512	8	10^{-4}	–	–	–	0.1	0	10^{-4}
TF _{shuffle}	1	–	512	8	10^{-4}	–	–	–	0.1	0.1	10^{-4}
TF _{set}	3	–	512	2	10^{-4}	–	0.5	10^{-3}	0.1	0.1	10^{-4}
LSTM	–	–	2 048	–	10^{-4}	–	–	–	0.1	0.5	10^{-4}
LSTM _{shuffle}	–	–	2 048	–	10^{-3}	–	–	–	10^{-2}	0.5	0
LSTM _{set}	–	–	2 048	–	10^{-4}	–	0.1	0.5	10^{-2}	0.5	0
FF _{BCE}	–	0	2 048	–	10^{-3}	–	–	–	10^{-2}	0.5	10^{-4}
FF _{BCE,C}	–	1	2 048	–	10^{-4}	10^{-2}	–	–	0.1	0.3	0
FF _{BCE,DC}	–	0	2 048	–	10^{-3}	1	–	–	10^{-2}	0.3	0
FF _{sIoU}	–	2	2 048	–	10^{-4}	–	–	–	0.1	0	10^{-4}
FF _{sIoU,C}	–	2	2 048	–	10^{-4}	10^{-2}	–	–	0.1	0.1	10^{-4}
FF _{TD}	–	3	512	–	10^{-3}	–	–	–	10^{-2}	0	0
FF _{TD,C}	–	3	512	–	10^{-4}	0.1	–	–	0.1	0	10^{-4}

Table 7: Hyperparameter values chosen by Hyperband for VOC. Here, w_C refers to the weight for the cardinality loss, l_r to the learning rate, and scale refers to the ratio between the image encoder’s and set predictor’s learning rates.

Model	L_t	L_f	embedding size	n_{att}	l_r	w_C	λ_{eos}	λ_{CP}	scale	dropout rate	weight decay
TF	3	—	256	4	10^{-3}	—	—	—	10^{-2}	0.1	10^{-4}
TF _{shuffle}	3	—	256	8	10^{-3}	—	—	—	10^{-2}	0	0
TF _{set}	2	—	512	2	10^{-4}	—	0.1	0	10^{-2}	0.1	0
LSTM	—	—	1024	—	10^{-3}	—	—	—	10^{-2}	0.1	10^{-4}
LSTM _{shuffle}	—	—	2048	—	10^{-4}	—	—	—	0.1	0	10^{-4}
LSTM _{set}	—	—	2048	—	10^{-4}	—	0.1	1	0.1	0.5	0
FF _{BCE}	—	1	256	—	10^{-4}	—	—	—	0.1	0.1	0
FF _{BCE,C}	—	2	1024	—	10^{-4}	10^{-2}	—	—	0.1	0	0
FF _{BCE,DC}	—	2	512	—	10^{-4}	1	—	—	0.1	0.3	0
FF _{sIoU}	—	1	2048	—	10^{-4}	—	—	—	0.1	0	0
FF _{sIoU,C}	—	1	2048	—	10^{-4}	10^{-3}	—	—	0.1	0	0
FF _{TD}	—	3	512	—	10^{-3}	—	—	—	10^{-2}	0	0
FF _{TD,C}	—	3	1024	—	10^{-4}	0.1	—	—	0.1	0.1	10^{-4}

Table 8: Hyperparameter values chosen by Hyperband for COCO. Here, w_C refers to the weight for the cardinality loss, l_r to the learning rate, and scale refers to the ratio between the image encoder’s and set predictor’s learning rates.

Model	L_t	L_f	embedding size	n_{att}	l_r	w_C	λ_{eos}	λ_{CP}	scale	dropout rate	weight decay
TF	3	—	256	8	10^{-4}	—	—	—	10^{-2}	0.1	10^{-4}
TF _{shuffle}	3	—	256	4	10^{-4}	—	—	—	0.1	0.3	0
TF _{set}	3	—	256	4	10^{-3}	—	10^{-2}	10^{-2}	10^{-2}	0	0
LSTM	—	—	1024	—	10^{-4}	—	—	—	10^{-2}	0.1	10^{-4}
LSTM _{shuffle}	—	—	1024	—	10^{-4}	—	—	—	0.1	0.5	10^{-4}
LSTM _{set}	—	—	1024	—	10^{-4}	—	10^{-2}	0	10^{-2}	0	0
FF _{BCE}	—	1	512	—	10^{-4}	—	—	—	10^{-2}	0.3	0
FF _{BCE,C}	—	0	1024	—	10^{-3}	0.1	—	—	10^{-2}	0.3	0
FF _{BCE,DC}	—	1	1024	—	10^{-4}	1	—	—	10^{-2}	0.3	0
FF _{sIoU}	—	1	2048	—	10^{-4}	—	—	—	0.1	0	0
FF _{sIoU,C}	—	1	1024	—	10^{-4}	10^{-3}	—	—	0.1	0	0
FF _{TD}	—	2	2048	—	10^{-3}	—	—	—	0.1	0.3	0
FF _{TD,C}	—	3	2048	—	10^{-4}	0.5	—	—	0.1	0.3	10^{-4}

Table 9: Hyperparameter values chosen by Hyperband for NUS-WIDE. Here, w_C refers to the weight for the cardinality loss, l_r to the learning rate, and scale refers to the ratio between the image encoder’s and set predictor’s learning rates.

Model	L_t	L_f	embedding size	n_{att}	l_r	w_C	λ_{eos}	λ_{CP}	scale	dropout rate	weight decay
TF	1	—	256	4	10^{-3}	—	—	—	0.1	0.1	10^{-4}
TF _{shuffle}	2	—	256	8	10^{-3}	—	—	—	0.1	0.1	0
TF _{set}	3	—	256	2	10^{-3}	—	10^{-2}	0.5	10^{-2}	0	0
LSTM	—	—	2048	—	10^{-3}	—	—	—	10^{-2}	0.3	10^{-4}
LSTM _{shuffle}	—	—	512	—	10^{-3}	—	—	—	0.1	0	0
LSTM _{set}	—	—	2048	—	10^{-4}	—	10^{-2}	0.5	0.1	0.5	0
FF _{BCE}	—	0	1024	—	10^{-2}	—	—	—	10^{-2}	0.1	0
FF _{BCE,C}	—	0	2048	—	10^{-3}	10^{-2}	—	—	10^{-2}	0.1	10^{-4}
FF _{BCE,DC}	—	3	2048	—	10^{-4}	1	—	—	0.1	0.1	0
FF _{sIoU}	—	1	2048	—	10^{-4}	—	—	—	0.1	0	0
FF _{sIoU,C}	—	1	2048	—	10^{-4}	10^{-3}	—	—	0.1	0	0
FF _{TD}	—	1	2048	—	10^{-2}	—	—	—	10^{-2}	0.1	0
FF _{TD,C}	—	2	2048	—	10^{-3}	10^{-2}	—	—	0.1	0.1	0

Table 10: Hyperparameter values chosen by Hyperband for ADE20k. Here, w_C refers to the weight for the cardinality loss, l_r to the learning rate, and scale refers to the ratio between the image encoder’s and set predictor’s learning rates.

Model	L_t	L_f	embedding size	n_{att}	l_r	w_C	λ_{eos}	λ_{CP}	scale	dropout rate	weight decay
TF	1	—	2048	8	10^{-4}	—	—	—	0.1	0.3	10^{-4}
TF _{shuffle}	2	—	256	4	10^{-3}	—	—	—	0.1	0.1	0
TF _{set}	2	—	2048	8	10^{-4}	—	10^{-3}	10^{-3}	0.1	0.5	0
LSTM	—	—	2048	—	10^{-4}	—	—	—	0.1	0.5	10^{-4}
LSTM _{shuffle}	—	—	2048	—	10^{-3}	—	—	—	0.1	0.1	10^{-4}
LSTM _{set}	—	—	256	—	10^{-3}	—	10^{-3}	0.1	10^{-2}	0.1	0
FF _{BCE}	—	2	2048	—	10^{-3}	—	—	—	10^{-2}	0	0
FF _{BCE,C}	—	3	2048	—	10^{-3}	10^{-3}	—	—	10^{-2}	0.1	0
FF _{BCE,DC}	—	2	1024	—	10^{-3}	1	—	—	10^{-2}	0.3	0
FF _{sIoU}	—	1	2048	—	10^{-4}	—	—	—	0.1	0.1	0
FF _{sIoU,C}	—	1	1024	—	10^{-3}	0.1	—	—	10^{-2}	0	0
FF _{TD}	—	3	1024	—	10^{-4}	—	—	—	0.1	0	10^{-4}
FF _{TD,C}	—	2	2048	—	10^{-3}	10^{-3}	—	—	0.1	0	0

Table 11: Hyperparameter values chosen by Hyperband for Recipe1M. Here, w_C refers to the weight for the cardinality loss, l_r to the learning rate, and scale refers to the ratio between the image encoder’s and set predictor’s learning rates.

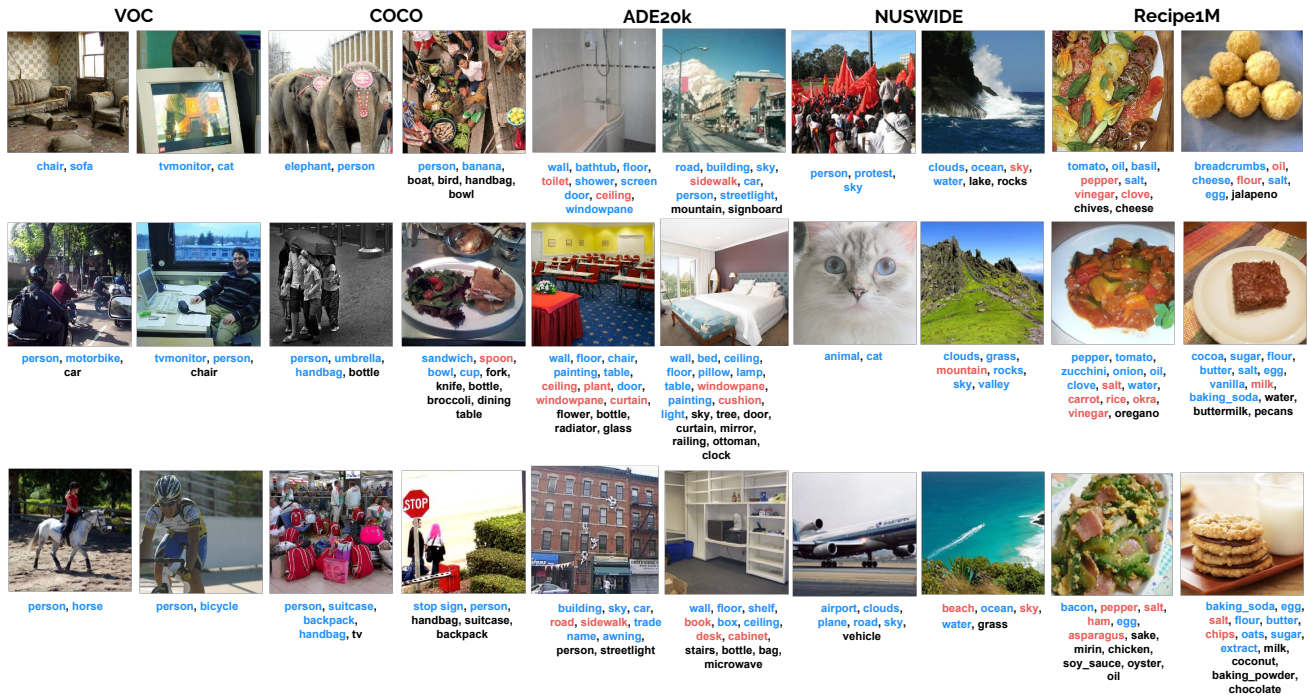


Figure 6: Additional qualitative results. Each column includes 6 examples for each dataset. True positives, false positives and false negatives are highlighted in blue, red and black, respectively.

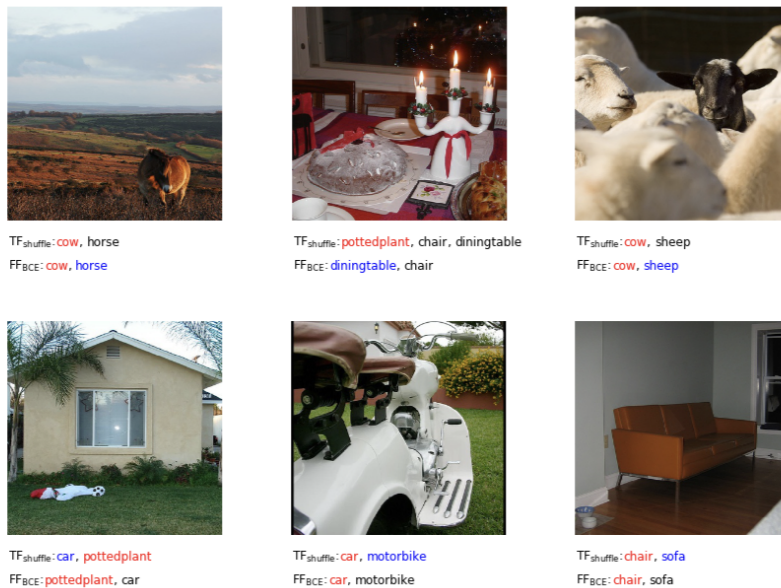


Figure 7: Qualitative comparison of models TF_{shuffle} and FF_{BCE} on VOC. Top row shows the 3 images where FF_{BCE} got the most improvement on I-F1 over TF_{shuffle} . The bottom row shows the 3 images where the converse situation occurs.

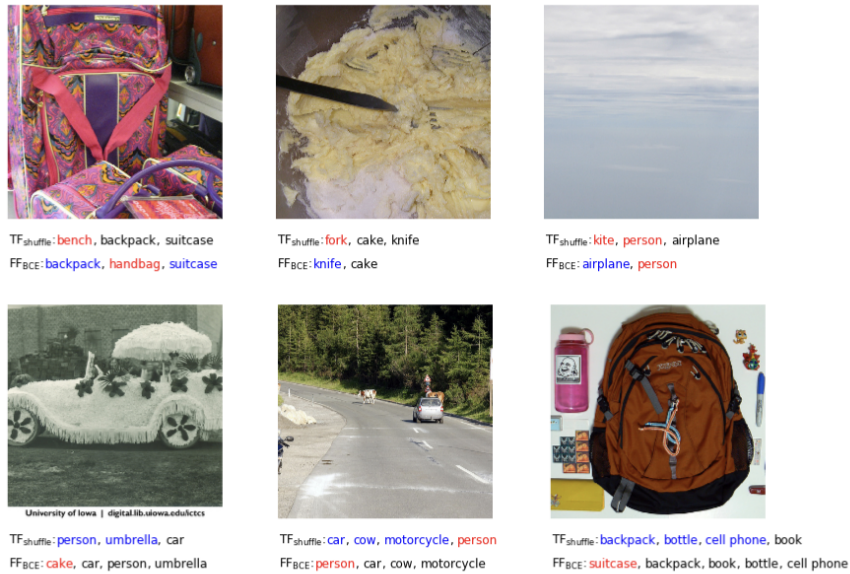


Figure 8: Qualitative comparison of models TF_{shuffle} and FF_{BCE} on COCO. Top row shows the 3 images where FF_{BCE} got the most improvement on I-F1 over TF_{shuffle} . The bottom row shows the 3 images where the converse situation occurs.

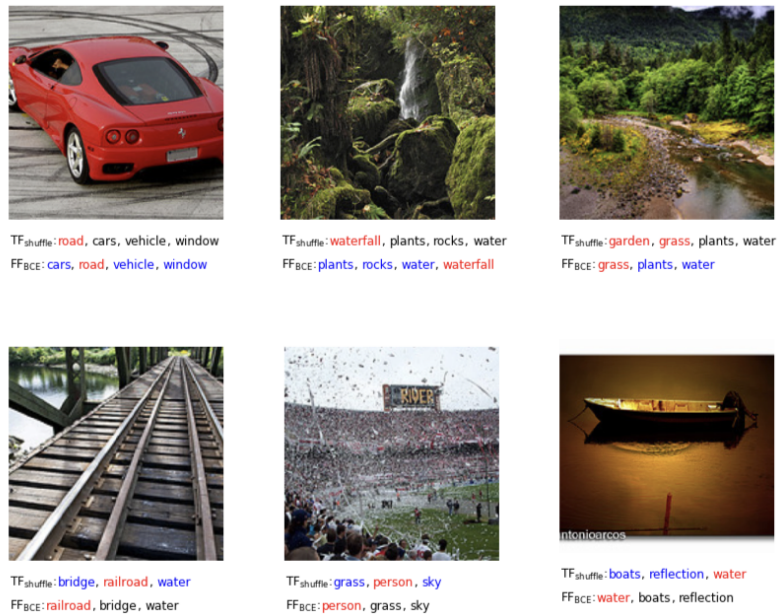


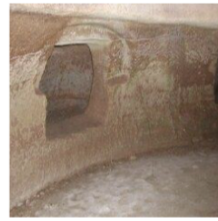
Figure 9: Qualitative comparison of models TF_{shuffle} and FF_{BCE} on NUS-WIDE. Top row shows the 3 images where FF_{BCE} got the most improvement on I-F1 over TF_{shuffle} . The bottom row shows the 3 images where the converse situation occurs.



TF_{shuffle}: building, car, pole, road, signboard, bus, person.
 FF_{BCE}: bus, road, windowpane, building, person, sidewalk



TF_{shuffle}: light, wall, ceiling, floor
 FF_{BCE}: ceiling, floor, light, wall



TF_{shuffle}: earth, sky, ceiling, floor, wall
 FF_{BCE}: floor, wall, ceiling



TF_{shuffle}: bannister, building, floor, tree, wall, water, sky
 FF_{BCE}: building, floor, tree, wall, sky, water



TF_{shuffle}: ceiling, floor, wall, road
 FF_{BCE}: wall, ceiling, road



TF_{shuffle}: ceiling, column, floor, wall, windowpane
 FF_{BCE}: building, earth, ceiling, column, floor, wall

Figure 10: Qualitative comparison of models TF_{shuffle} and FF_{BCE} on ADE20k. Top row shows the 3 images where FF_{BCE} got the most improvement on I-F1 over TF_{shuffle}. The bottom row shows the 3 images where the converse situation occurs.



TF_{shuffle}: butter, cheese, roll, egg, flour, salt, sugar, water, yeast
 FF_{BCE}: butter, flour, salt, sugar, water, yeast, egg



TF_{shuffle}: cheese, pepperoni, pizza_dough, pizza_sauce, flour, oil, rosemary, salt, water, yeast
 FF_{BCE}: cheese, flour, oil, salt, water, yeast, rosemary



TF_{shuffle}: chicken, dove, ginger, pepper, rice, soy_sauce, sugar
 FF_{BCE}: cheese, chicken, dove, ginger, rice, soy_sauce, sugar



TF_{shuffle}: butter, cheese, flour, milk, onion, pepper, potato, salt, water
 FF_{BCE}: oil, butter, cheese, flour, milk, onion, pepper, potato, salt, water

Figure 11: Qualitative comparison of models TF_{shuffle} and FF_{BCE} on Recipe1M. Top row shows the 3 images where FF_{BCE} got the most improvement on I-F1 over TF_{shuffle}. The bottom row shows the 3 images where the converse situation occurs.

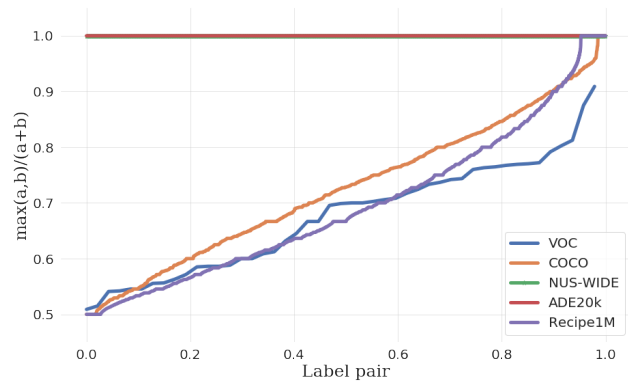


Figure 12: Order in label pairs.

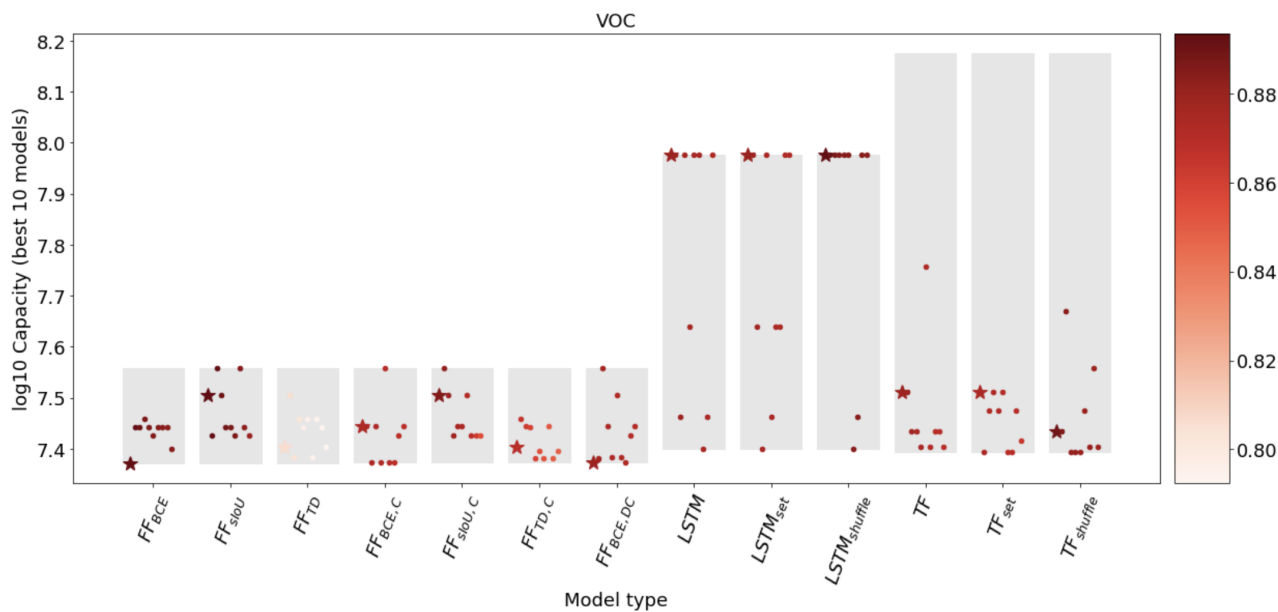


Figure 13: Capacity of best 10 models found by Hyperband, for each model class, in the VOC dataset. Each point corresponds to a combination of hyperparameter values, and the y -axis is the base-10 log of the total number of parameters. Grey rectangles represent the range of model capacities that was considered for a model during tuning. Color scale of the points represents best O-F1 over validation set. Within a box, models are shown in decreasing order of O-F1 score, from left to right.

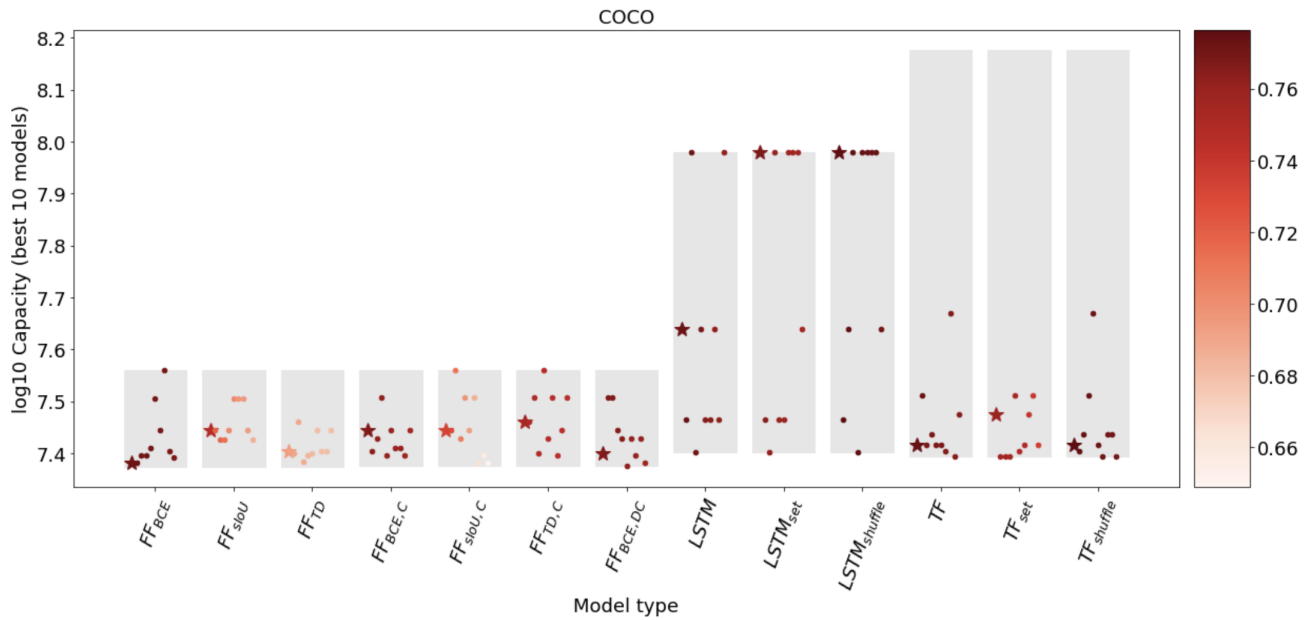


Figure 14: Capacity of best 10 models found by Hyperband, for each model class, in the COCO dataset. Each point corresponds to a combination of hyperparameter values, and the y -axis is the base-10 log of the total number of parameters. Grey rectangles represent the range of model capacities that was considered for a model during tuning. Color scale of the points represents best O-F1 over validation set. Within a box, models are shown in decreasing order of O-F1 score, from left to right.

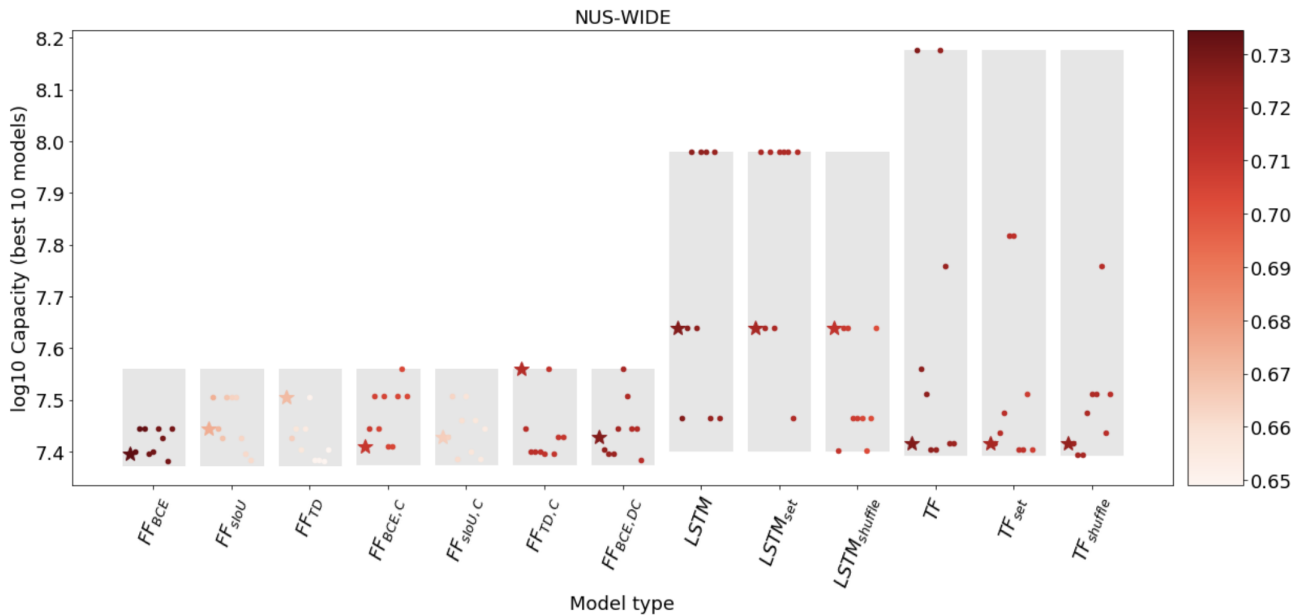


Figure 15: Capacity of best 10 models found by Hyperband, for each model class, in the NUS-WIDE dataset. Each point corresponds to a combination of hyperparameter values, and the y -axis is the base-10 log of the total number of parameters. Grey rectangles represent the range of model capacities that was considered for a model during tuning. Color scale of the points represents best O-F1 over validation set. Within a box, models are shown in decreasing order of O-F1 score, from left to right.

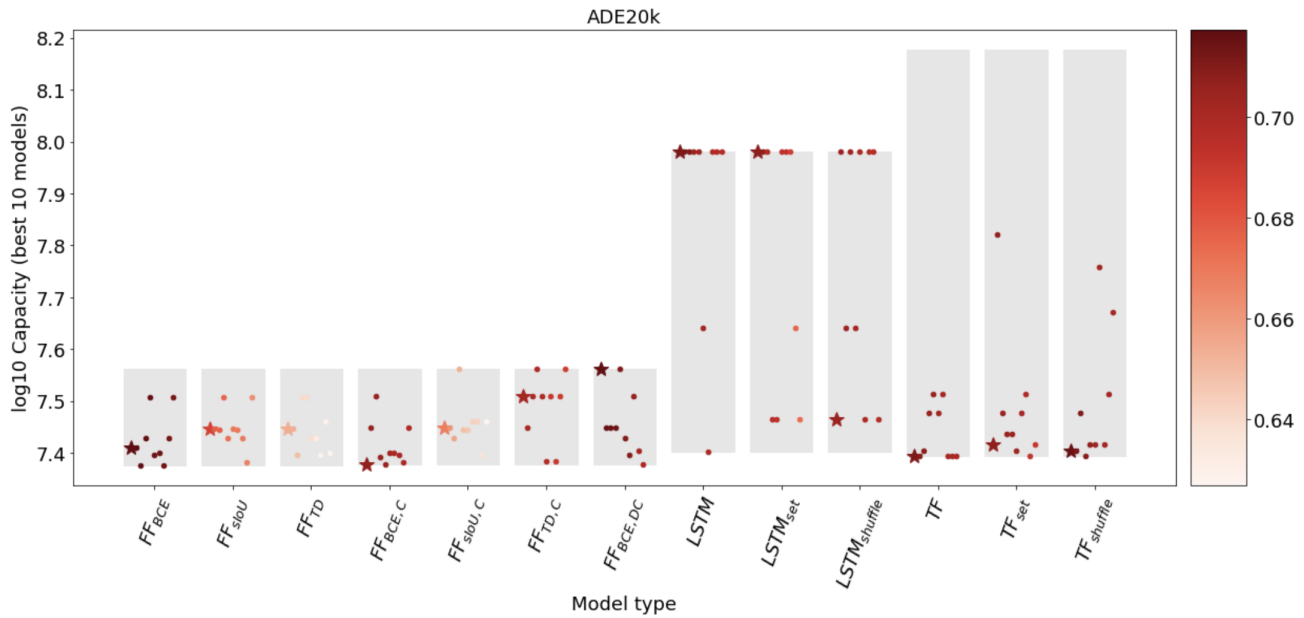


Figure 16: Capacity of best 10 models found by Hyperband, for each model class, in the ADE20k dataset. Each point corresponds to a combination of hyperparameter values, and the y -axis is the base-10 log of the total number of parameters. Grey rectangles represent the range of model capacities that was considered for a model during tuning. Color scale of the points represents best O-F1 over validation set. Within a box, models are shown in decreasing order of O-F1 score, from left to right.

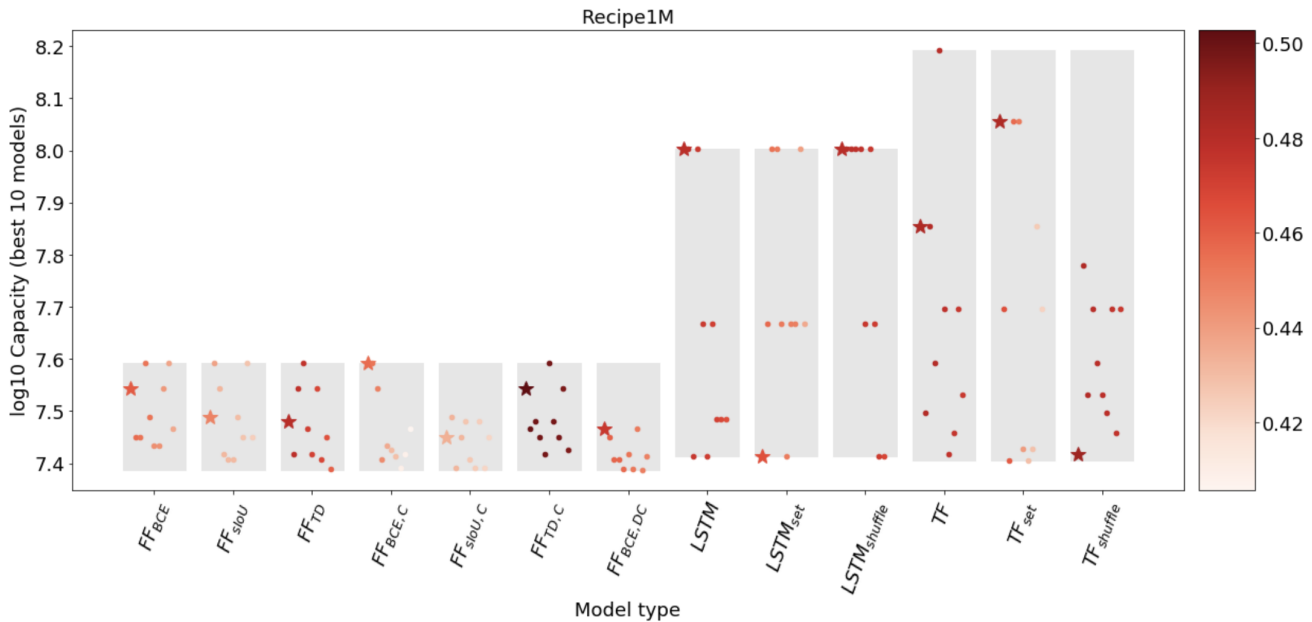


Figure 17: Capacity of best 10 models found by Hyperband, for each model class, in the Recipe1M dataset. Each point corresponds to a combination of hyperparameter values, and the y -axis is the base-10 log of the total number of parameters. Grey rectangles represent the range of model capacities that was considered for a model during tuning. Color scale of the points represents best O-F1 over validation set. Within a box, models are shown in decreasing order of O-F1 score, from left to right.